PCCP

Accepted Manuscript

ROYAL SOCIETY OF CHEMISTRY

www.rsc.org/pccp

Encapsulation of an *f*-block metal atom/ion to enhance the stability of C_{20} with the I_h symmetry

Fanchen Meng[a,b] Zuowan Zhou[a,*] Pinliang Zhang[a] Man Jiang[a] Xiaoling Xu[a] Yong Wang[a] Jihua Gou[a,c] David Hui[d] Dong Die[e,f]

[a] Key Laboratory of Advanced Technologies of Materials (Ministry of Education), School of Materials Science and Engineering, Southwest Jiaotong University, Chengdu, 610031, PR China

[b] Department of Physics and Astronomy, Clemson University, Clemson, South Carolina, 29631, United States

[c] Department of Mechanical, Materials and Aerospace Engineering, University of Central Florida, Orlando, Florida 32816, United States

[d] Department of Mechanical Engineering, University of New Orleans, New Orleans, Louisiana 70148, United States

[e] Key Laboratory of Advanced Scientific Computation, Xihua University, Chengdu 610039, China

[f] School of Physics and Chemistry, Xihua University, Chengdu 610039, China

Abstract

Based on the density functional theory, the geometric and electronic structures, chemical stability, and bonding properties of the endohedral metallofullerenes, M@C_{20} (M=Eu^{3-}, Am^{3-}, Gd^{2-}, Cm^{2-}, Tb^{-}, Bk^{-}, Dy, Cf, Ho^{+}, Es^{+}, Er^{2+}, Fm^{2+}, Tm^{3+}, Md^{3+}, Yb^{4+}, No^{4+}, Lu^{5+}, and Lr^{5+}), were investigated. Through encapsulation of an *f*-block metal atom/ion with 12 valence electrons, the bare C_{20} cage with D_{2h} point

* corresponding author: Tel/Fax: +86 28 8760 0454. E-mail: zwzhou@at-c.net (Z. Zhou).

group could be stabilized to a highly symmetrical I_h structure. The calculated values of HOMO–LUMO energy gap using the B3LYP and BHHLYP functionals ranged from 2.22 to 5.39 eV and from 3.89 to 7.95 eV, respectively. The stability of these metal-encapsulated clusters can be attributed to the 32-electron rule, where the central metal atom's orbitals strongly participated in the t_{2u}, g_u, t_{1u}, h_g, and a_g valence molecular orbitals.

1. Introduction

Because of the three hybridizations of carbon (sp, sp^2, and sp^3), different types of allotropes can be formed, making it a fundamental element in nature. However, graphite and diamond, with sp^2- and sp^3-hybridized carbons, respectively, are the only two naturally occurring allotropes. Thus, it has been a challenge in material science and technology to discover and synthesize new carbon allotropes either alone or as a combination of these hybridization states. [1–5] At the end of 20^{th} century, C_{60} fullerene has been successfully synthesized. [3] Thus, cluster science has attracted considerable attention [6–35] because of its importance in designing new materials. Consequently, fullerene and its derivatives provide a group of potential materials with novel structural and electronic properties, such as covalent bonding, high chemical reactivity, large steric strain, and superconductivity. [36–38] In particular, smaller fullerenes are of special interest because of the presence of high curvature and large strain energy caused by the adjacent pentagonal rings, resulting in unusual intra- and intermolecular bonding and electronic properties. Recently, after observing the shell structure of the smallest fullerene $M@C_{28}$ (M = Ti, Zr, and U), [39] the search for highly stable smaller fullerenes has gained tremendous momentum, e.g., $U@C_{36}$, [39,

40] U@C_{44}, [39] U@C_{28}, [6, 30, 39] M@C_{26}, [41] (M = lanthanide/actinide atoms/ions), and M@C_{20} [34] (M = lanthanide/actinide atoms/ions).

In the past decades, it has been demonstrated that the chemical stability of a particular cluster (either metallic or nonmetallic) can be enhanced significantly by encapsulating an impurity atom [6, 8–10, 30]. In general, the origin of the high stability of a particular cluster may be electronic or geometric. The electronic origin can be considered as a manifestation of electronic shell closing [8, 42, 43] and thus can explain the higher intensity of a particular cluster than its neighbors in a cluster abundance spectrum. Similar shell closing for atomic systems is well known in chemistry by varying the chemical properties of elements across the periodic table. Similarly, the highly symmetric geometric closed-shell structure can be considered as one of the important factors for the higher stability of a particular size cluster.

C_{20} is the smallest fullerene that may have the highest symmetry (I_h), corresponding to a triplet state with a four-fold degenerate highest occupied molecular orbital (HOMO). However, due to the Jahn–Teller distortion, the I_h structure of C_{20} is distorted to D_{5d} or C_{5v} structure. Further, these structures continually reduce to a lower symmetry because of the presence of a two-fold degenerate triplet state. [44] Finally, a nondegenerate singlet state with the D_{3d}, D_{2h}, or C_{2h} symmetry becomes the ground-state structure for the C_{20} cage. [44–46] Therefore, it is interesting to study whether or not C_{20} with the I_h symmetry could be stabilized. Recently, neutral Ce@C_{20} and Gd@C_{20} clusters and 3d transition metal atom encapsulated C_{20} clusters have been studied theoretically. [47-49] These clusters have C_{2h} symmetry, which is much lower than the I_h symmetry, probably because of the absence of a magic number electron configuration. Recently, Manna *et al*. theoretically predicted a new series of M@C_{20} [34] (M = Pr^-, Pa^-, Nd, U, Pm^+, Np^+, Sm^{2+}, Pu^{2+}, Eu^{3+}, Am^{3+}, Gd^{4+}, and Cm^{4+})

clusters, a 26-electron system with the I_h symmetry, and explained their enhanced stability from the aspect of a large HOMO–LUMO energy gap, large binding energy, etc.

In this study, our objective was to investigate the possibility of stabilizing the C_{20} cage into the highest symmetry, namely I_h, by encapsulating suitable metal atom/ion from the *f*-block elements (Eu^{3-}, Am^{3-}, Gd^{2-}, Cm^{2-}, Tb^{-}, Bk^{-}, Dy, Cf, Ho^{+}, Es^{+}, Er^{2+}, Fm^{2+}, Tm^{3+}, Md^{3+}, Yb^{4+}, No^{4+}, Lu^{5+}, and Lr^{5+}) so that the total number of valence electrons corresponds to the 32-electron rule with a closed-shell configuration as indicated by Langmuir in 1921. [50] To the best of our knowledge, a system satisfying 32-valence electrons corresponding to the centrally located atom in C_{20} cluster has not yet been reported.

2. Computational details

The calculations were performed using the widely used Gaussian 09. [51] The geometries of the bare C_{20} cage and M@C_{20} clusters (M = Eu^{3-}, Am^{3-}, Gd^{2-}, Cm^{2-}, Tb^{-}, Bk^{-}, Dy, Cf, Ho^{+}, Es^{+}, Er^{2+}, Fm^{2+}, Tm^{3+}, Md^{3+}, Yb^{4+}, No^{4+}, Lu^{5+}, and Lr^{5+}) were optimized by the density functional theory (DFT). To investigate the exchange correlation effect, the BP86, [55, 56] PBE (written as PBE1PBE in Gaussian 09), [57, 58] PBE0, [59] BHHLYP, [60] B3PW91 [61, 62] and B3LYP [61, 63] functionals were used in all cases. For metal atom/ion, the Stuttgart energy-adjusted, small-core RECP (SDD) [52] as implemented in Gaussian 09 was combined with the associated SDD basis set, also included in Gaussian 09. (Note that the most diffuse primitive for each shell, each with an exponent of 0.005, was removed to obtain proper convergence of the electronic density.) For carbon atom, an all-electron basis set with polarization functions, i.e., the 6-31G(d) basis set, was used. The combination of DFT

with small-core RECPs has been shown to provide good results for lanthanide and actinide systems at a reasonable computational cost. [47, 53, 54]

To understand the charge reorganization due to the formation of the M@C_{20} cluster from M and C_{20} species, the partial atomic charges were calculated using the Löwdin and Hirsfeld schemes as implemented in the Multiwfn program. [64] The Voronoi deformation density (VDD) [65] charges were calculated from the flow of electron density to or from a certain atom or fragment due to the bond formation, thus evaluating the charge rearrangements due to the formation of the complex between the lanthanide or actinide atom/ion and C_{20} fragments. Moreover, using the Multiwfn program, the quantum theory of atoms in molecules (QTAIM) [66] bonding analysis was performed to determine the critical points and bond paths, and the electron localization function (ELF) was calculated to analyze the bonding between carbon and metal atom/ion.

The bonding properties were also studied from the aspect of energetics, namely, binding energy (BE). The binding energy was obtained from the complex geometries of the corresponding atomic dissociation channel. Thus, for a M@C_{20} cluster, the BE can be calculated as follows:

$$BE = 20 \times E(C) + E(M) - E(M@C_{20}) \quad (1)$$

where $E(M@C_{20})$ is the total energy of the complex at the equilibrium geometry. $E(C)$ and $E(M)$ are the energies of the carbon and metal atom/ion, respectively.

3. Results and discussion

3.1 Geometry Optimization

In this study, the geometries of the bare C_{20} cage and all the $M@C_{20}$ clusters were optimized using different functionals as implemented in Gaussian 09. To verify whether the structures are true minima on their respective potential energy surfaces, the vibrational frequencies were also calculated at the same theoretical level as in the geometrical calculation. In all cases, the geometry optimization led to the highly symmetric closed-shell I_h structure, even though the geometries of $M@C_{20}$ clusters were optimized starting from the various initial cage structures. Figure 1 shows the optimized structures of the bare C_{20} and $M@C_{20}$ clusters. The encapsulated metal atom/ion preferred to locate at the center of the C_{20} cage in all the $M@C_{20}$ clusters, as shown in Figure 1.

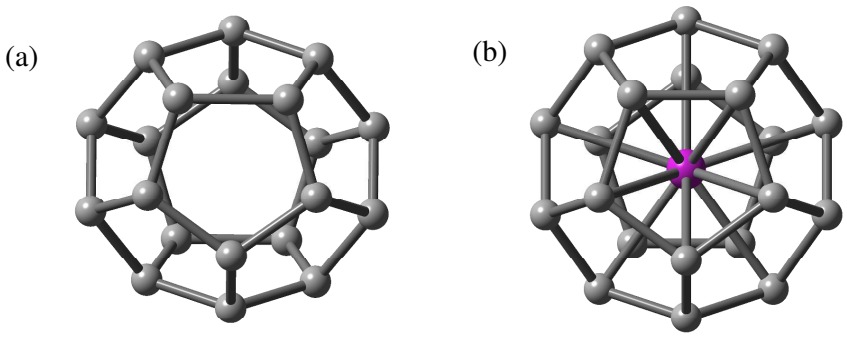

Figure 1 Optimized structures (a) the bare C_{20} cage and (b) $M@C_{20}$ clusters with M = Eu^{3-}, Am^{3-}, Gd^{2-}, Cm^{2-}, Tb^{-}, Bk^{-}, Dy, Cf, Ho^{+}, Es^{+}, Er^{2+}, Fm^{2+}, Tm^{3+}, Md^{3+}, Yb^{4+}, No^{4+}, Lu^{5+}, and Lr^{5+}.

From now onwards, the results obtained using the B3LYP functional are considered unless otherwise stated. Because of the uncertainty of the ground state of

the bare C_{20} cluster, [44–46] in this study, the C_{20} cages with different symmetries, such as D_{3d}, D_{2h}, and C_{2h}, were involved in the calculation. The structure with D_{2h} symmetry was found to be the ground-state (with the lowest energy) structure for the bare C_{20} cluster, and the electronic state of the D_{2h}-C_{20} was ^1A_g state, in accordance with the previous report [46]. Notably, the energy differences among the D_{2h}, D_{3d}, and C_{2h} structures were almost negligible. However, the search for the ground state of the bare C_{20} cluster is beyond the scope of this study. After the encapsulation of metal atom/ion with 12 valence electrons, all the systems were highly symmetrical I_h structure. The incorporation of metal atom/ion within the C_{20} cage overall increased the cage size, and the C–C bond distances, as listed in Table 1, slightly increased to 1.522–1.562 Å, compared to the bare D_{2h}-C_{20} cage whose C–C bond distances lie in the range 1.445–1.537 Å. In general, the extent of increase was smaller for the positively charged metal ions when compared with negatively charged metal ions, and was larger for the actinide series compared to the lanthanide series. To investigate the effect of different functionals apart from the B3LYP functional, the B3PW91, BHHLYP, BP86, PBE0, and PBE functionals were also used in optimizing the geometries of the bare C_{20} and M@C_{20} clusters. The C–C and M–C bond lengths obtained using different functionals are listed in Table 1. For a certain metal atom/ion, the bond lengths calculated using different functionals were almost the same. The trends in the variation of the C–C and M–C bond lengths along the lanthanide and actinide series also remain the same. In general, the C–C and M–C bond lengths decreased from Eu to Ho and increased from Er to Lu in the lanthanide series. In the actinide series, a similar trend for the M–C bond length was observed, namely, decreasing from Am to Es and increasing from Er to Lu.

Table 1 Calculated M–C Bond Distance (R_{M-C} in Å) and C–C Bond Distance (R_{M-C} in Å) Using Different Functionals for All M@C_{20} Clusters

Metal atom/ion	R_{M-C} in Å						R_{C-C} in Å					
	B3LYP	B3PW91	BHHLYP	BP86	PBE0	PBE	B3LYP	B3PW91	BHHLYP	BP86	PBE0	PBE
Eu^{3-}	2.176	2.165	2.164	2.188	2.159	2.182	1.553	1.545	1.544	1.561	1.541	1.557
Gd^{2-}	2.159	2.147	2.144	2.168	2.143	2.162	1.541	1.532	1.530	1.547	1.529	1.543
Tb^{-}	2.144	a	2.126	b	2.127	2.149	1.530	a	1.517	b	1.518	1.534
Dy	2.134	2.124	a	b	2.118	b	1.523	1.516	a	b	1.512	b
Ho^{+}	2.133	2.123	2.110	2.144	2.117	2.139	1.522	1.515	1.506	1.530	1.511	1.526
Er^{2+}	2.132	2.122	2.110	2.144	2.117	2.138	1.522	1.515	1.505	1.530	1.511	1.526
Tm^{3+}	2.137	2.127	2.115	2.148	2.122	2.143	1.525	1.518	1.509	1.533	1.514	1.529
Yb^{4+}	2.146	2.136	2.126	2.156	2.131	2.151	1.532	1.524	1.517	1.539	1.521	1.535
Lu^{5+}	2.158	2.148	2.138	2.167	2.143	2.162	1.540	1.533	1.526	1.547	1.529	1.543
Am^{3-}	2.189	2.177	2.166	2.203	2.169	2.196	1.562	1.554	1.546	1.572	1.548	1.567
Cm^{2-}	2.171	2.159	2.152	2.185	2.153	2.178	1.549	1.541	1.536	1.559	1.536	1.554
Bk^{-}	2.158	2.146	2.138	2.170	2.140	2.165	1.540	1.531	1.526	1.549	1.527	1.545
Cf	2.145	2.134	2.125	2.157	2.128	2.151	1.531	1.523	1.516	1.539	1.518	1.535
Es^{1+}	2.142	2.131	2.121	2.152	2.125	2.147	1.528	1.521	1.513	1.536	1.517	1.532
Fm^{2+}	2.144	2.133	2.123	2.153	2.127	2.148	1.530	1.522	1.515	1.537	1.518	1.533
Md^{3+}	2.149	2.138	2.128	2.159	2.132	2.153	1.534	1.526	1.519	1.541	1.522	1.537
No^{4+}	2.162	2.151	2.142	2.171	2.145	2.165	1.543	1.535	1.528	1.549	1.530	1.545
Lr^{5+}	2.175	2.164	2.155	2.184	2.159	2.178	1.552	1.545	1.538	1.558	1.540	1.554

[a]values are not reported because imaginary frequencies were found [b]values are not reported due to bad convergence

3.2 Chemical Stability

The effect of encapsulation and chemical stability can be evaluated by the HOMO–LUMO energy difference and binding energy. The calculated values of the

HOMO–LUMO energy gaps using different functionals are listed in Table 2. For a particular cluster, HOMO–LUMO gap value calculated using the BHHLYP was the largest among all, resulting from 50% contribution of HF exchange in this hybrid functional. The HOMO–LUMO energy gap obtained with the B3LYP functional for the bare C_{20} cage with D_{2h} symmetry was 1.94 eV, which was very close to the previously calculated value of 1.93 eV. [46] Compared to the bare C_{20} cluster (1.94 eV with the B3LYP functional), the calculated value of HOMO–LUMO energy gap for all of the endohedral clusters were significantly higher (e.g., 2.22–5.39 eV at the same theoretical level). In general, the HOMO–LUMO energy gap increased with increasing positive charge of the encapsulated metal atom/ion. These two trends were valid for all the functionals considered in this study. Therefore, after the incorporation of metal atom/ion into the C_{20} cage, the improvement in chemical stability was confirmed. A similar trend in the calculated HOMO–LUMO energy gap for certain highly stable systems has been reported. [8–11, 13, 14, 27–30] According to previous reports, spin-orbital coupling support the conclusion on the 32-electron principle for this type of systems, namely, encapsulated clusters. [28–30, 34, 41, 67] Therefore, in this study, spin-orbital effect was not taken into account.

Table 2 Calculated HOMO–LUMO Energy Gap Values (in eV) Using Different Functionals for All M@C_{20} Clusters

Metal atom/ion	B3LYP	B3PW91	BHHLYP	BP86	PBE0	PBE
Eu^{3-}	2.64	2.83	3.89	1.11	3.12	1.04
Gd^{2-}	3.32	3.44	5.32	1.25	3.77	1.26
Tb^{-}	2.53	a	5.87	b	3.48	1.45
Dy	3.69	3.93	a	b	4.57	b
Ho^{+}	4.22	4.31	6.70	2.04	4.74	1.98
Er^{2+}	4.26	4.36	6.74	2.23	4.79	2.19
Tm^{3+}	4.55	4.65	7.12	2.61	5.10	2.58
Yb^{4+}	5.08	5.22	7.10	3.39	5.60	3.38
Lu^{5+}	4.92	5.07	6.91	3.71	5.43	3.76
Am^{3-}	3.02	3.09	5.34	1.70	3.47	1.74
Cm^{2-}	2.22	2.28	4.37	1.46	2.54	1.26
Bk^{-}	3.91	3.93	6.77	1.94	4.51	1.97
Cf	4.67	4.65	7.31	2.24	5.33	2.28
Es^{1+}	5.39	5.39	7.95	2.72	5.99	2.75
Fm^{2+}	5.22	5.23	7.46	3.20	5.61	3.21
Md^{3+}	5.21	5.25	7.33	3.74	5.62	3.76
No^{4+}	5.00	5.05	7.01	3.67	5.40	3.68
Lr^{5+}	4.88	4.93	6.90	3.57	5.28	3.58
C_{20} (D_{2h})	1.94	1.93	3.77	0.74	2.23	0.73

[a]values are not reported because imaginary frequencies were found [b]values are not reported due to bad convergence

It is of great interest to examine the binding energies of the clusters with respect to atomic fragments because these types of clusters are generally obtained from the constituent atomic fragments (produced by the laser ablation of the corresponding solid materials). [6, 9, 27] Therefore, the binding energy of a metal-encapsulated

cluster with respect to its atomic fragments was calculated by using equation (1). The calculated values of the binding energy are listed in Table 3. Herein, BE is the dissociation energy of a complex (into its atomic fragments) and refers to the process: $M + 20 \times C \rightarrow M@C_{20}$. Notably, a positive value for the binding energy indicates a stable cluster. All the endohedral clusters were highly stable regarding their dissociation into the constituent atomic fragments with the binding energy range from 96 to 270 eV (with the B3LYP functional). All the actinide-containing species, except $Md^{3+}@C_{20}$, were more stable than the corresponding lanthanide-encapsulated clusters.

Table 3 Calculated Zero-Point Energy Corrected Binding Energy Values (in eV) Using Different Functionals for All M@C_{20} Clusters

Metal atom/ion	Binding Energy					
	B3LYP	B3PW91	BHHLYP	BP86	PBE0	PBE
Eu^{3-}	115.13	120.57	106.39	130.18	122.66	133.42
Gd^{2-}	108.34	114.07	102.01	120.30	116.67	123.42
Tb^{-}	95.55	a	87.30	b	103.60	115.85
Dy	97.17	103.25	a	b	105.18	b
Ho^{+}	108.14	113.84	94.64	123.20	115.83	126.79
Er^{2+}	109.68	115.19	96.30	124.23	117.13	128.04
Tm^{3+}	270.44	274.96	252.17	287.39	275.64	289.89
Yb^{4+}	143.63	148.89	130.78	157.68	150.91	161.28
Lu^{5+}	185.91	191.09	174.10	199.13	193.21	202.66
Am^{3-}	121.44	127.25	110.16	135.53	129.62	138.93
Cm^{2-}	114.94	121.33	104.78	130.80	123.62	132.89
Bk^{-}	115.69	122.09	105.29	129.88	124.57	133.55
Cf	112.94	119.43	101.71	127.42	121.85	131.14
Es^{1+}	112.08	118.31	100.19	126.49	120.70	130.29
Fm^{2+}	112.31	118.21	100.17	126.57	120.60	130.30
Md^{3+}	120.67	126.35	108.72	134.55	128.65	138.15
No^{4+}	158.21	163.13	146.97	171.02	166.12	174.55
Lr^{5+}	175.66	181.05	165.34	188.18	183.45	191.65

[a]values are not reported because imaginary frequencies were found [b]values are not reported due to bad convergence

3.3 Bonding Analysis

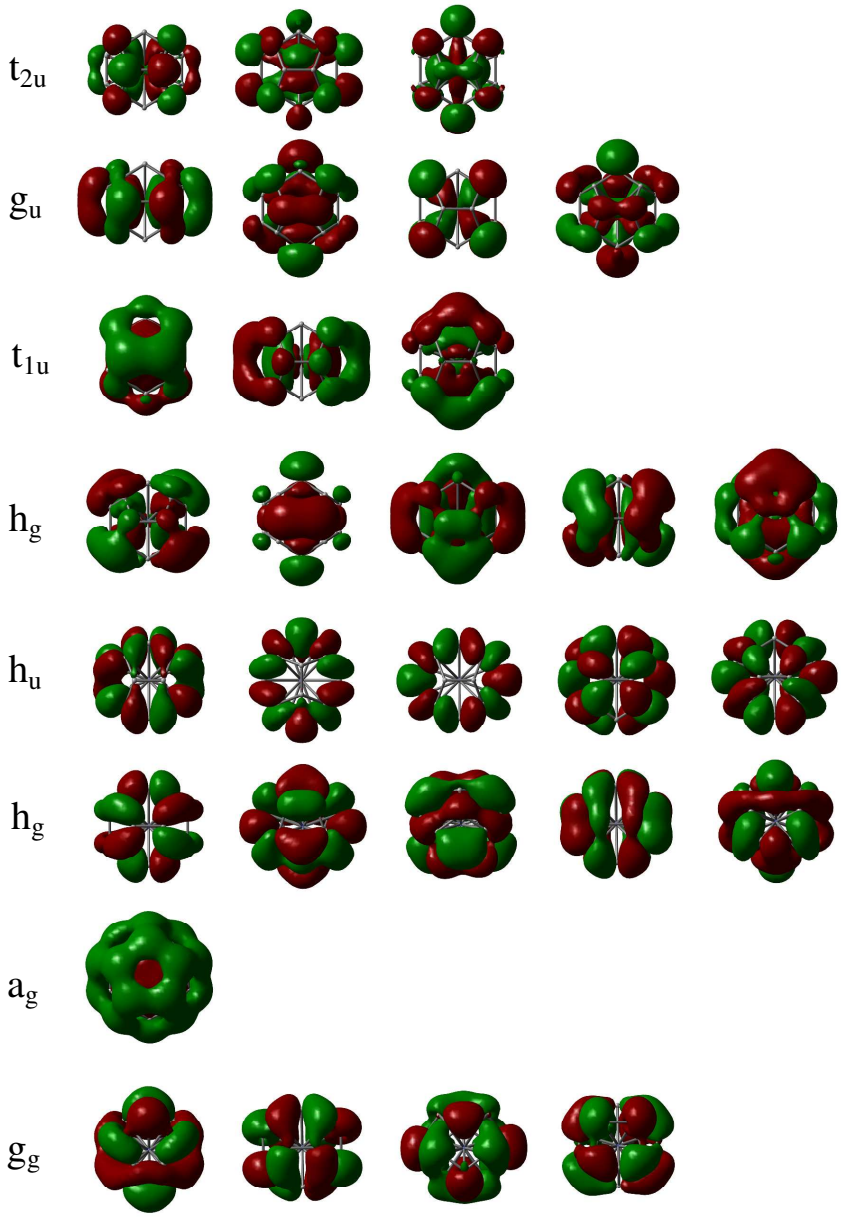

Figure 2 Valence molecular orbitals for $Am^{3-}@C_{20}$.

The $Am^{3-}@C_{20}$ valence molecular orbitals (MOs) are shown in the descending energetic order in Figure 2. The overlap between the Am^{3-} atomic orbitals and the C_{20}

cage orbitals in the t_{2u}, g_u, t_{1u}, h_g, and a_g valence MOs, resulting from strong participation of the central atom orbitals in these 16 MOs, with 32 valence electrons. The other MOs are the bare C_{20} cage orbitals that do not interact with the metal center. Therefore, clearly all the 7s, 7p, 6d, and 5f orbitals of the Am^{3-} ion hybridize with 2p orbitals of the C_{20} cage. However, not all metal atom/ion encapsulated clusters follow the molecular order, namely, the descending energetic order from t_{2u} to a_g, as shown in Figure 2. This order could only be applied to the Eu^{3-}, Am^{3-}, Cm^{2-}, Bk^{-}, and Cf encapsulated C_{20} clusters. In Gd^{2-}, Tb^{-}, Dy, and Es^{2+} clusters, the g_u MO becomes the HOMO while the other MOs remain the same. However, the valence MOs not discussed above were quite "disordered" for the endohedral clusters, namely, Ho^{+}, Er^{2+}, Tm^{3+}, Yb^{4+}, Lu^{5+} in the lanthanide series and Fm^{2+}, Md^{3+}, No^{4+}, and Lr^{5+} in the actinide series. To better understand the electronic structures of these clusters, explaining the chemical stability and bonding properties of the endohedral clusters, the MO energy diagram of these clusters calculated using the B3LYP functional is shown in Figure 3. Because the MO energy diagrams of the $Ho^{+}@C_{20}$ and $Er^{2+}@C_{20}$ are of the same energetic order, the MO energy diagram of $Ho^{+}@C_{20}$ is not shown in Figure 3. With increasing positive charge of the encapsulated metal atom/ion, the bands of all the endohedral clusters shifted downward to more negative energy because of the stronger bonding between the metal atom/ion and C_{20} cage. In general, this may explain the increase in the binding energies of these clusters with the accumulation of the positive charge on the central atom/ion. The orbital composition analysis with Ros–Schuit (SCPA) partition was used to analyze the MOs of $Am^{3-}@C_{20}$ (Figure 2), thus providing a useful description of their character. The contributions per MO are the largest for the 5f atomic orbitals: 56% and 42% for the t_{2u} and g_u MOs, respectively. The t_{1u} and h_g MOs also mix the 7p and 6d orbitals with

the 2p orbitals of the carbon atoms of the cage. The a_g MO corresponds to the 7s orbital hybridizing with the cage. Further, with increasing positive charge of the encapsulated metal atom/ion, more f contributions were found. Therefore, the s, p, and d contributions decreased slightly as more positive charges accumulated on the central metal atom/ion. Therefore, the lanthanide and actinide atoms/ions corresponding to 12 valence electrons were able to elevate the D_{2h} symmetry of the C_{20} cage to the I_h symmetry by fulfilling the 32-electron principle for the encapsulated metal atom/ion. In fact, only few chemical systems fulfilling the 32-electron rule with a high stability have been predicted so far. [28–30, 41, 67]

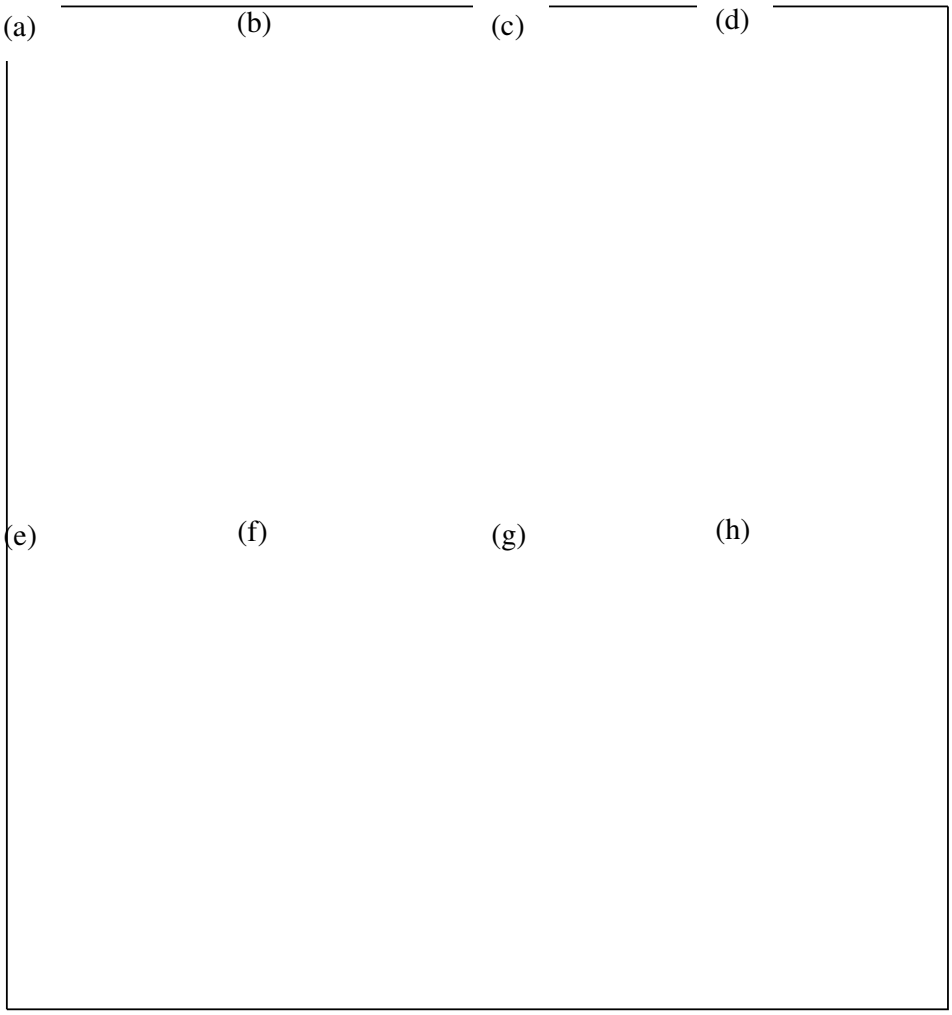

Figure 3 Occupied valence orbital energy levels for (a) $Er^{2+}@C_{20}$, (b) $Tm^{3+}@C_{20}$, (c) $Yb^{4+}@C_{20}$, (d) $Lu^{5+}@C_{20}$, (e) $Fm^{2+}@C_{20}$, (f) $Md^{3+}@C_{20}$, (g) $No^{4+}@C_{20}$, and (h) $Lr^{5+}@C_{20}$ clusters.

Next, the charge distributions in the $M@C_{20}$ clusters were analyzed. The calculated Löwdin, VDD, and Hirshfeld charges on the central metal atom/ion using different functionals are listed in Table 4. High negative charges were obtained on the metal centers by the Löwdin charge analysis, as listed in Table 4. However, the high negative values of the atomic charges on the metal centers obtained from the

orbital-based population analysis schemes, namely, Löwdin, particularly for the positively charged clusters are somewhat unrealistic. The VDD method is based on the calculated amount of electronic density that flows to or from a certain atom due to the bond formation through the spatial integration of the deformation density over the atomic Voronoi cell and thus is not explicitly dependent on the basis functions involved in a calculation. In this manner, the VDD analysis, which was used to understand the charge rearrangements due to the formation of the $Am^{3-}@C_{20}$ clusters from its constituent fragments, can provide realistic charges. Therefore, the charges obtained from the VDD analysis were also calculated apart from the Löwdin schemes. Consequently, the VDD derived charges are considered to provide chemically meaningful charge distributions in a chemical system. The calculated VDD charges (Table 4) lie in the range from –0.11 to –0.34 and provide chemically meaningful values.

Table 4 Calculated Löwdin, VDD, and Hirshfeld Charges on Metal Centers Using Different Functionals for All M@C_{20} Clusters

Metal atom/ion	Löwdin			VDD			Hirsfeld		
	B3LYP	BHHLYP	PBE0	B3LYP	BHHLYP	PBE0	B3LYP	BHHLYP	PBE0
Eu^{3-}	–4.237	–4.301	–4.487	0.178	0.220	0.193	0.020	0.038	0.017
Gd^{2-}	–4.309	–4.355	–4.559	0.045	0.509	0.047	–0.014	0.397	–0.032
Tb^{-}	–4.306	–4.408	–4.564	–0.105	–0.160	0.185	–0.213	–0.297	0.050
Dy	–4.471	a	–4.471	0.108	a	0.108	0.099	a	0.099
Ho^{+}	–4.284	–4.461	–4.519	0.171	0.239	0.181	0.199	0.256	0.205
Er^{2+}	–4.256	–4.463	–4.480	0.149	0.149	0.155	0.212	0.212	0.217
Tm^{3+}	–4.113	–4.335	–4.335	0.150	0.120	0.166	0.241	0.219	0.258
Yb^{4+}	–3.898	–4.108	–4.111	0.200	0.145	0.203	0.310	0.265	0.315
Lu^{5+}	–2.503	–2.628	–2.640	–0.026	–0.055	–0.030	0.107	0.084	0.100
Am^{3-}	–6.843	–7.062	–6.981	0.339	0.372	0.373	0.049	0.041	0.057
Cm^{2-}	–5.765	–5.885	–5.885	–0.069	0.377	–0.044	–0.203	0.203	–0.199
Bk^{-}	–4.078	–4.096	–4.229	0.206	0.294	0.237	0.128	0.186	0.134
Cf	–3.310	–3.355	–3.456	0.241	0.315	0.267	0.203	0.251	0.209
Es^{1+}	–3.135	–3.221	–3.281	0.229	0.261	0.248	0.222	0.236	0.221
Fm^{2+}	–5.678	–5.797	–5.812	0.137	0.130	0.153	0.184	0.166	0.184
Md^{3+}	–2.139	–2.262	–2.271	0.199	0.672	0.212	0.268	0.683	0.263
No^{4+}	–1.379	–1.517	–1.490	0.263	0.196	0.274	0.340	0.273	0.334
Lr^{5+}	–2.305	–2.371	–2.372	–0.001	–0.050	–0.182	0.165	0.102	0.034

[a]values are not reported because imaginary frequencies were found [b]values are not reported due to bad convergence

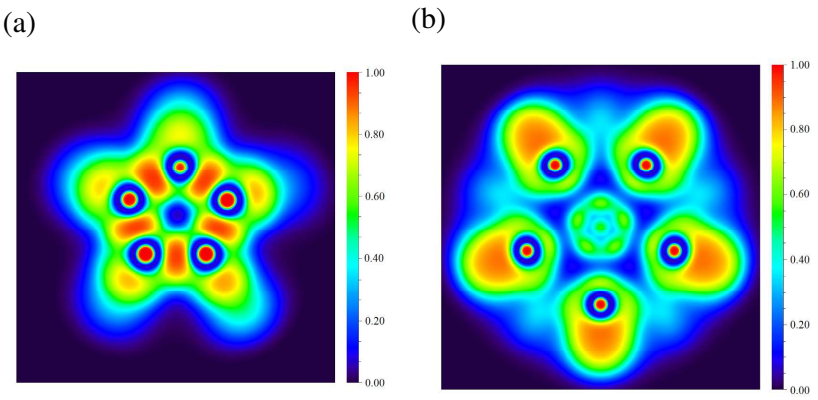

Figure 4 Cut-plane ELF representations for (a) the bare C_{20} cage and (b) the $Am^{3+}@C_{20}$ cluster.

The cut-plane ELF representations are shown in Figure 4. The various ELF representations differ strongly from the bare C_{20} cluster to the $Am^{3-}@C_{20}$ cluster. For the bare C_{20} cage, the basins are located around the carbon atoms, and a large hole can be observed in the center of the empty cage. However, for the Am^{3-} encapsulated cluster, a local electron accumulation area existed between the central atom and C atoms of the cage, indicating strong bonding. Similar results were found for all the lanthanide and actinide endohedral clusters. To examine the bond type between the metal atom/ion and carbon atoms of the C_{20} cage, the topological analyses of the electron density [68, 69] were performed. According to Bader [70] and Matta [71], in the QTAIM, atoms are considered as "chemically bonded" when their nuclei are linked by the bond path, which is a single line of local maximum density. Further, when they shared a bond critical point (BCP), which is the minimum electron density along the bond path, atoms are also believed to be "chemically bonded". In addition, a ring critical point (RCP) was always found in the interior of the ring of chemically bonded atoms. [71] Further, a cage critical point (CCP) appears in the enclosed space

when several rings are connected in a manner enclosing the interstitial space. [71] Figure 5 shows the molecular graph (i.e., the set of bond paths and critical points) of the $Am^{3-}@C_{20}$ cluster.

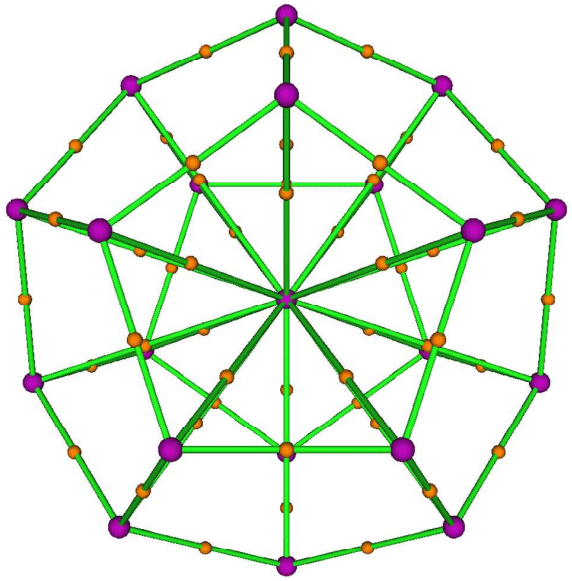

Figure 5 AIM molecular graph of the $Am^{3-}@C_{20}$ cluster. Green points represent bond critical points, green lines represent bond paths.

The electron and energy densities at the C–M BCPs calculated with different functionals are listed in Table 5 and they are almost the same. In all the clusters, a significant accumulation of electron density was observed between the carbon atom and metal atoms/ions with negative energy density, indicating an electron-shared interaction (i.e., covalent). [72] For example, in $Am^{3-}@C_{20}$ cluster, the value of the electron density at the BCP calculated with the B3LYP functional was 0.114 e/Bohr^3 per C–Am^{3-} interaction. The corresponding value of the energy density calculated at

the same theoretical level for all the C–Am^{3-} BCPs were –0.034 hartree/$Bohr^3$. These results not only confirmed the ELF analyses presented above in finding significant bonding between carbon atoms and metal atom/ion, but also confirmed that the bonding is covalent, explaining the large binding energy of these endohedral clusters.

Table 5 Calculated Electron Density and Energy Density Using Different Functionals for All M@C_{20} Clusters

Metal atom/ion	Electron Density (e/$Bohr^3$)			Energy Density (hartree/ $Bohr^3$)		
	B3LYP	BHHLYP	PBE0	B3LYP	BHHLYP	PBE0
Eu^{3-}	0.100	0.102	0.106	–0.034	–0.035	–0.040
Gd^{2-}	0.105	0.108	0.110	–0.037	–0.041	–0.043
Tb^{-}	0.107	0.113	0.113	–0.039	–0.045	–0.045
Dy	0.109	a	0.115	–0.041	a	–0.047
Ho^{+}	0.106	0.113	0.111	–0.039	–0.045	–0.045
Er^{2+}	0.103	0.110	0.109	–0.037	–0.043	–0.043
Tm^{3+}	0.100	0.105	0.105	–0.035	–0.040	–0.040
Yb^{4+}	0.095	0.099	0.100	–0.032	–0.036	–0.036
Lu^{5+}	0.092	0.096	0.097	–0.029	–0.033	–0.034
Am^{3-}	0.114	0.118	0.120	–0.047	–0.051	–0.054
Cm^{2-}	0.116	0.120	0.122	–0.048	–0.052	–0.055
Bk^{-}	0.118	0.123	0.124	–0.049	–0.054	–0.055
Cf	0.119	0.125	0.125	–0.053	–0.059	–0.059
Es^{1+}	0.119	0.125	0.125	–0.052	–0.059	–0.059
Fm^{2+}	0.117	0.123	0.123	–0.051	–0.057	–0.057
Md^{3+}	0.112	0.117	0.118	–0.045	–0.050	–0.051
No^{4+}	0.106	0.111	0.112	–0.041	–0.045	–0.047
Lr^{5+}	0.102	0.106	0.107	–0.039	–0.042	–0.044

[a]values are not reported because imaginary frequencies were found

4. Conclusions

In this study, by encapsulating an actinide or lanthanide atom/ion, a new class of closed-shell clusters of the smallest fullerene, $M@C_{20}$, was proposed. Based on DFT, the geometric and electronic structures, chemical stability, and bonding properties of the endohedral clusters were investigated. Both highly symmetric (I_h) structure and large HOMO–LUMO energy gap indicated that the $M@C_{20}$ clusters were highly stable than the bare D_{2h}-C_{20} cage. The high stability arises from the hybridization between the valence MOs of the carbon atoms and metal atoms/ions, satisfying the 32-electron rule. Therefore, these clusters qualify as new examples of 32-electron species. Mass or photoelectron spectroscopy may be one of the possible methods for detecting the elusive I_h structure of the C_{20} cage, which may be prepared using laser ablation techniques, as reported earlier for the $U@C_n$ clusters.

Acknowledgement

We appreciate Professor Sir Harold Kroto from Florida State University and Dr. Chris Ewels from Universite de Nantes for their academic suggestions and discussions. This work was financially supported by the National Natural Science Foundation of China (Nos. 51173148, 51303151, 51302230), the Science and Technology Planning Project of Sichuan Province (Nos. 2013RZ0036, 2011GZX0052), and the Fundamental Research Funds for the Central Universities of China (polymer research project).

Reference

1 Balaban AT, Rentia CC, Ciupitu E. Chemical Graphs.VI Estimation of relative stability of several planar and tridimensional lattices for elementary carbon. Rev Roum Chim 1968;13(2):231-247.

2 Diederich F. Carbon scaffolding: building acetylenic all-carbon and carbon-rich compounds. Nature 1994;369(6477):199-207.

3 Kroto HW, Heath J, O'brien SC, Curl RF, Smalley RE. C_{60}: Buckminsterfullerene. Nature 1985;318:162-163.

4 Iijima S. Helical microtubules of graphitic carbon. Nature 1991;354:56-58.

5 Novoselov KS, Geim AK, Morozov SV, Jiang D, Zhang Y, Dubonos SV, et al. Electric Field Effect in Atomically Thin Carbon Films. Science 2004;306(5696):666-669.

6 Guo T, Diener MD, Chai Y, Alford MJ, Haufler RE, McClure SM, et al. Uranium Stabilization of C_{28}: A Tetravalent Fullerene. Science 1992;257(5077):661-1664.

7 Khanna SN, Jena P. Assembling crystals from clusters. Phys Rev Lett 1992;71(1): 208(E)-1.

8 Pyykkö P, Runeberg N. Icosahedral WAu_{12}: A Predicted Closed-Shell Species, Stabilized by Aurophilic Attraction and Relativity and in Accord with the 18-Electron Rule. Angew Chem 2002;114(12):2278-2280.

9 Li X, Kiran B, Li J, Zhai HJ; Wang LS. Experimental observation and confirmation of icosahedral W@ Au_{12} and Mo@ Au_{12} molecules. Angew Chem Int Ed 2002;41(24):4786-4789.

10 Autschbach J, Hess BA, Johansson MP, Neugebauer J, Patzschke M, Pyykkö P, et al. Properties of WAu_{12}. Phys Chem Chem Phys 2004;6(1):11-22.

11 Li J, Li X, Zhai HJ, Wang LS. Au_{20}: A tetrahedral cluster. Science 2003;299(5608):864-867.

12 Ghanty TK, Chandrakumar KRS, Ghosh SK. Magic clusters MAu_4 (M= Ti and Zr) and their dimers: How magic are they? J Chem Phys 2004;120(24):11363-11366.

13 Johansson M P, Sundholm D, Vaara J. Au_{32}: A 24-Carat Golden Fullerene. Angew Chem Int Ed 2004;43(20):2678-2681.

14 Gao Y, Bulusu S, Zeng XC. Gold-caged metal clusters with large HOMO-LUMO gap and high electron affinity. J Am Chem Soc 2005;127(45):15680-15681.

15 Karttunen AJ, Linnolahti M, Pakkanena TA, Pyykkö P. Icosahedral Au_{72}: a predicted chiral and spherically aromatic golden fullerene. Chem Commun 2008;(4):465-467.

16 Bergeron DE, Roach PJ, Castleman Jr AW, Jones NO, Khanna SN. Al cluster superatoms as halogens in polyhalides and as alkaline earths in iodide salts. Science 2005;307(5707):231-235.

17 Castleman Jr AW, Jena P. Clusters: A bridge across the disciplines of environment, materials science, and biology. Proc Natl Acad Sci 2006;103(28):10554-10559.

18 Reveles JU, Khanna SN, Roach PJ, Castleman Jr AW. Multiple valence superatoms. Proc Natl Acad Sci 2006;103(49):18405-18410.

19 Wang LM, Bulusu S, Zhai HJ, Zeng XC, Wang LS. Doping Golden Buckyballs: Cu@Au16$^-$ and Cu@Au17$^-$ Cluster Anions. Angew Chem Int Ed 2007;46(16):2915-2918.

20 Reveles JU, Clayborne PA, Reber AC, Khanna SN, Pradhan K, Sen P, et al. Designer magnetic superatoms. Nat Chem 2009;1(4):310-315.

21 Huang W, Sergeeva AP, Zhai HJ, Averkiev BB, Wang LS, Boldyrev AI. A concentric planar doubly π-aromatic B_{19}^- cluster. Nat Chem 2010;2(3):202-206.

22 Köster AM, Calaminici P, Orgaz E, Roy DR, Reveles JU, Khanna SN. On the ground state of Pd_{13}. J Am Chem Soc 2011;133(31):12192-12196.

23 Medel VM, Reveles JU, Khanna SN, Chauhan V, Sen P, Castleman AW. Hund's rule in superatoms with transition metal impurities. Proc Natl Acad Sci 2011;108(25):10062-10066.

24 Li WL, Romanescu C, Galeev TR, Piazza ZA, Boldyrev AI, Wang LS. Transition-Metal-Centered Nine-Membered Boron Rings: M©B_9 and M©B_9^- (M = Rh, Ir). J Am Chem Soc 2012;134(1):165-168.

25 Cui LF, Huang X, Wang LM, Boldyrev AI, Li J, Wang LS. Pb_{22}^-: Plumbaspherene. J Phys Chem A 2006;110(34):10169-10172.

26 Cui LF, Huang X, Wang LM, Zubarev DY, Boldyrev AI, Li J, et al. Sn_{22}^-: Stannaspherene. J Am Chem Soc 2006;128(26):8390-8391.

27 Cui LF, Huang X, Wang LM, Li J, Wang LS. Endohedral Stannaspherenes M@Sn^{12-}: A Rich Class of Stable Molecular Cage Clusters. Angew Chem Int Ed 2007;46(5):742-745.

28 Dognon JP, Clavaguéra C, Pyykkö P. Towards a 32-Electron Principle: $Pu@Pb_{12}$ and Related Systems. Angew Chem Int Ed 2007;46(9):1427-1430.

29 Dognon JP, Clavaguéra C, Pyykkö P. Chemical properties of the predicted 32-electron systems $Pu@Sn_{12}$ and $Pu@Pb_{12}$. Comp Rend Chim 2010;13(6):884-888.

30 Dognon JP, Clavaguéra C, Pyykkö P. A Predicted Organometallic Series Following a 32-Electron Principle: $An@C_{28}$ (An = Th, Pa^{+}, U^{2+}, Pu^{4+}). J Am Chem Soc 2009;131(1):238-243.

31 Johansson MP, Vaara J, Sundholm D. Exploring the stability of golden fullerenes. J Phys Chem C 2008;112(49):19311-19315.

32 Ghanty TK, Banerjee A, Chakrabarti A. Structures and the Electronic Properties of $Au_{19}X$ Clusters (X = Li, Na, K, Rb, Cs, Cu, and Ag). J Phys Chem C 2010;114(1):20-27.

33 Banerjee A, Ghanty TK, Chakrabarti A, Kamal C. Nonlinear Optical Properties of $Au_{19}M$ (M = Li, Na, K, Rb, Cs, Cu, Ag) Clusters. J Phys Chem C 2012;116(1):193-200.

34 Manna D, Ghanty TK. Theoretical Prediction of Icosahedral $U@C_{20}$ and Analogous Systems with High HOMO–LUMO Gap. J Phys Chem C 2012;116(31):16716-16725.

35 Jayasekharan T, Ghanty TK. Endohedrally Doped Golden Fullerenes [$X@Au_{32}$] (X = Li^{+}, Na^{+}, K^{+}, Rb^{+}, Cs^{+}) J Phys Chem C 2010;114(19):8787-8793.

36 Heath JR. Fullerenes: C_{60}'s Smallest Cousin. Nature 1998:393(6687):730-731.

37 Fowler PW, Mitchell D, Zerbetto F. C_{36}: The Best Fullerene for Covalent Bonding. J Am Chem Soc 1999;121(13):3218−3219.

38 Côte M, Grossman JC, Cohen ML, Louie SG. Electron Phonon Interactions in Solid C_{36}. Phys Rev Lett 1998;81(3):697-700.

39 Dunk PW, Kaiser NK, Mulet-Gas M, Rodriguez-Fortea A, Poblet JM, Shinohara H, et al. The Smallest Stable Fullerene, M@C_{28} (M = Ti, Zr, U): Stabilization and Growth from Carbon Vapor. J Am Chem Soc 2012;134(22):9380-9389.

40 Manna D, Ghanty TK. Enhancement in the Stability of 36-atom Fullerene through Encapsulation of a Uranium Atom. J Phys Chem C 2013;117(34):17859-17869.

41 Manna D, Ghanty TK. Prediction of a New Series of Thermodynamically Stable Actinide Encapsulated Fullerene Systems Fulfilling the 32-Electron Principle. J Phys Chem C 2012;116(48):25630-25641.

42 Knight WD, Clemenger K, de Heer WA, Saunders WA, Chou MY, Cohen ML. Electronic Shell Structure and Abundances of Sodium Clusters. Phys Rev Lett 1984;52(24):2141-2143.

43 Harbola MK. Magic Numbers for Metallic Clusters and the Principle of Maximum Hardness. Proc Natl Acad Sci 1992;89(3):1036-1039.

44 Paulus B. Electronic and structural properties of the cage-like molecules C_{20} to C_{36}. Phys Chem Chem Phys 2003;5(16):3364-3367.

45 An W, Geo Y, Bulusu S, Zeng XC. Ab initio calculation of bowl, cage, and ring isomers of C_{20} and C_{20}^{-}. J Chem Phys 2005;122(20):204109-8.

46 Zhang CJ, Sun WX, Cao ZX. Most stable structure of fullerene[20] and its novel activity toward addition of alkene: A theoretical study. J Chem Phys 2007;126(14):144306-7.

47 Wu J, Sun Z, Li X, Ma B, Tian M, Li S. Theoretical study on the smallest endohedral metallofullerenes: TM@ C_{20} (TM= Ce and Gd). Int J Quantum Chem 2011;111(14):3786-3792.

48 ŞAKIR E. Metal Atom Endohedrally Doped C_{20} Cage STRUCTURE:(X@ C 20; X= Ni, Fe, Co). International Journal of Modern Physics C 2005;16(10): 1553-1560.

49 Isha G, Hitesh S, Neha K, Keya D, Jindal VK. Transition metal induced magnetism in smaller fullerenes (C_n for n≤ 36). Nanoscale 2011;3(1): 217-224.

50 Langmuir I. Types of valence. Science 1921;54(1386):59-67.

51 Frisch MJ, Trucks GW, Schlegel HB, Scuseria GE, Robb MA, Cheeseman JR, et al. GAUSSIAN 09. A.01 ed. Wallingford, CT: Gaussian, Inc.; 2009.

52 Küchle W, Dolg M, Stoll H, Preuss H. Energy-adjusted pseudopotentials for the actinides. Parameter sets and test calculations for thorium and thorium monoxide. J Chem Phys 1994;100(10):7535-7542.

53 Shamov GA, Schreckenbach G, Vo TN. A Comparative Relativistic DFT and ab initio Study on the Structure and Thermodynamics of the Oxofluorides of Uranium (IV), (V) and (VI). Chem A Eur J 2007;13(17):4932-4947.

54 Batista ER, Martin RL, Hay PJ, Peralta JE, Scuseria GE. Density functional investigations of the properties and thermochemistry of UF_6 and UF_5 using

valence-electron and all-electron approaches. J Chem Phys 2004;121(5):2144-2150.

55 Becke AD. Density-functional exchange-energy approximation with correct asymptotic behavior. Phys Rev A 1988;38(6):3098-3100.

56 Perdew JP. Density-functional approximation for the correlation energy of the inhomogeneous electron gas. Phys Rev B 1986;33(12):8822-8824.

57 Perdew JP, Burke K, Ernzerhof M. Generalized Gradient Approximation Made Simple. Phys Rev Lett 1996;77(18):3865-3868.

58 Perdew JP, Burke K, Ernzerhof M. Generalized Gradient Approximation Made Simple. Phys Rev Lett 1997;78(7):1396 (E)-1.

59 Adamo C, Barone V. Toward reliable density functional methods without adjustable parameters: The PBE0 model. J Chem Phys 1999;110(13):6158-6170.

60 Becke AD. A new mixing of Hartree-Fock and local density‐functional theories. J Chem Phys 1993;98(2):1372-1377.

61 Becke AD. Density‐functional thermochemistry. III. The role of exact exchange. J Chem Phys 1993;98(7):5648-5652.

62 Perdew JP, Wang Y. Accurate and simple analytic representation of the electron-gas correlation energy. Phys Rev B 1992;45(23):13244-13249.

63 Lee C, Yang WT, Parr RG. Development of the Colle-Salvetti correlation-energy formula into a functional of the electron density. Phys Rev B 1988;37(2):785-789.

64 Lu T, Chen FW. Multiwfn: A multifunctional wavefunction analyzer. J Comp Chem 2012;33(5):580-592.

65 Guerra CF, Handgraaf JW, Baerends EJ, Bickelhaupt FM. Voronoi deformation density (VDD) charges: Assessment of the Mulliken, Bader, Hirshfeld, Weinhold, and VDD methods for charge analysis. J Comput Chem 2004;25(2):189-210.

66 Bader R. Atoms in Molecules: A Quantum Theory. Oxford: Oxford University Press; 1990.

67 Dognon JP, Clavaguérab C, Pyykkö P. A new, centered 32-electron system: the predicted $[U@Si_{20}]6^{-}$-like isoelectronic series. Chem Sci 2012;3(9):2843-2848.

68 Arnold PL, Turner ZR, Kaltsoyannis N, Pelekanaki P, Bellabarba RM, Tooze RP. Covalency in Ce^{IV} and U^{IV} Halide and N-Heterocyclic Carbene Bonds. Chem A Eur J 2010;16(31):9623-9629.

69 Blake MP, Kaltsoyannis N, Mountford P. Heterobimetallic complexes containing Ca-Fe or Yb-Fe bonds: synthesis and molecular and electronic structures of [M $\{CpFe(CO)_2\}_2(THF)_3]_2$ (M= Ca or Yb). J Am Chem Soc 2011;133(39):15358-15361.

70 Bader RFW. A bond path: a universal indicator of bonded interactions. J Phys Chem A 1998;102(37):7314-7323.

71 Matta C, Boyd R. An Introduction to the Quantum Theory of Atoms in Molecules. Weinheim: WILEY-VCH Verlag GmbH & Co. KGaA; 2007.

72 Cremer D, Kraka E. Chemical Bonds without Bonding Electron Density—Does the Difference Electron-Density Analysis Suffice for a Description of the Chemical Bond? Angew Chem Int Ed 1984;23(8):627-628.

Figure Captions

Figure 1 Optimized structures (a) the bare C_{20} cage and (b) M@C_{20} clusters with M = Eu^{3-}, Am^{3-}, Gd^{2-}, Cm^{2-}, Tb^{-}, Bk^{-}, Dy, Cf, Ho^{+}, Es^{+}, Er^{2+}, Fm^{2+}, Tm^{3+}, Md^{3+}, Yb^{4+}, No^{4+}, Lu^{5+}, and Lr^{5+}.

Figure 2 Valence molecular orbitals for Am^{3-}@C_{20}.

Figure 3 Occupied valence orbital energy levels for (a) Er^{2+}@C_{20}, (b) Tm^{3+}@C_{20}, (c) Yb^{4+}@C_{20}, (d) Lu^{5+}@C_{20}, (e) Fm^{2+}@C_{20}, (f) Md^{3+}@C_{20}, (g) No^{4+}@C_{20}, and (h) Lr^{5+}@C_{20} clusters.

Figure 4 Cut-plane ELF representations for (a) the bare C_{20} cage and (b) the Am^{3+}@C_{20} cluster.

Figure 5 AIM molecular graph of the Am^{3-}@C_{20} cluster. Green points represent bond critical points, green lines represent bond paths.

Table Captions

Table 1 Calculated M–C Bond Distance (R_{M-C} in Å) and C–C Bond Distance (R_{M-C} in Å) Using Different Functionals for All M@C_{20} Clusters

Table 2 Calculated HOMO–LUMO Energy Gap Values (in eV) Using Different Functionals for All M@C_{20} Clusters

Table 3 Calculated Zero-Point Energy Corrected Binding Energy Values (in eV) Using Different Functionals for All M@C_{20} Clusters

Table 4 Calculated Löwdin, VDD, and Hirshfeld Charges on Metal Centers Using Different Functionals for All M@C_{20} Clusters

Table 5 Calculated Electron Density and Energy Density Using Different Functionals for All M@C_{20} Clusters